

Light emission from silicon with tin-containing nanocrystals

Søren Roesgaard,¹ Jacques Chevallier,^{1,2} Peter I. Gaiduk,³ John Lundsgaard Hansen,^{1,2} Pia Bomholt Jensen,^{1,2} Arne Nylandsted Larsen,^{1,2} Axel Svane,² Peter Balling,^{1,2} and Brian Julsgaard^{1,2}

¹*Interdisciplinary Nanoscience Center (iNANO), Aarhus University, Gustav Wieds Vej 14, DK-8000 Aarhus C, Denmark.*

²*Department of Physics and Astronomy, Aarhus University, Ny Munkegade 120, DK-8000 Aarhus C, Denmark.*

³*Belarussian State University, Praspjyekt Nyezalyezhnastsi 4, 220030 Minsk, Belarus.*

(Dated: 22 September 2021)

Tin-containing nanocrystals, embedded in silicon, have been fabricated by growing an epitaxial layer of $\text{Si}_{1-x-y}\text{Sn}_x\text{C}_y$, where $x = 1.6\%$ and $y = 0.04\%$ on a silicon substrate, followed by annealing at various temperatures ranging from 650°C to 900°C . The nanocrystal density and average diameters are determined by scanning transmission-electron microscopy to $\approx 10^{17}\text{ cm}^{-3}$ and $\approx 5\text{ nm}$, respectively. Photoluminescence spectroscopy demonstrates that the light emission is very pronounced for samples annealed at 725°C , and Rutherford back-scattering spectrometry shows that the nanocrystals are predominantly in the diamond-structured phase at this particular annealing temperature. The origin of the light emission is discussed.

It is a long-lasting desire to combine electrical and optical functionality in silicon (Si)¹, the achievement of which is hindered mainly by the indirect band gap of Si. In order that light can be manipulated and trapped inside Si, the photon energy must be well below the Si band-gap energy, which has led researchers to investigate light emission from various combinations of the other group-IV elements, carbon (C), germanium (Ge), and tin (Sn). One possible route is to use Ge, which is also an indirect-band-gap material, but the direct band gap can be approached by strain engineering². The combination of tensile strain and high doping has led to the demonstration of lasing in Ge³. Another line of research includes Sn in the material, and in addition to the strain conditions, the capability of efficient light emission now also depends on the relative composition of Ge and Sn^{4,5}. A proper choice of parameters has recently led to the demonstration of light-emitting diodes⁶ and lasing⁷ in GeSn alloys. In general, it is possible to combine C, Si, Ge, and Sn in epitaxial film-growth processes due to strain symmetrization⁸, and the accessible parameter space becomes very large. For instance, a broad-band luminescence peak at 0.77 eV has been observed from SiSn films⁹, and this emission can be enhanced by adding a small amount of carbon¹⁰. In the present work, we follow yet another strategy: embedding nanocrystals containing Sn inside crystalline silicon. Diamond-structured α -Sn is a direct-band-gap material in bulk form, and the optical transition is predicted to remain strong in the nanocrystal regime¹¹. In general, light emission is also possible from nanocrystals of indirect-band-gap materials due to the break-down of the momentum-conservation rule¹², and, in addition, size control enables tuning of the emission energy. In the longer perspective, an efficient nanosized light emitter might work as a single-photon source¹³ in Si. The successful embedding of Sn nanocrystals in Si has been realized by a number of research groups¹⁴⁻¹⁸, but studies of light emission is very limited. Recently, new spectral features were reported in the infrared region from Sn nanocrystals in SiGe quantum wells¹⁷, and

previously¹⁶ a broad luminescence peak around 0.85 eV was observed but not investigated in further detail. In this work, we obtain a similar luminescence peak as in the latter reference, and we demonstrate that its strength is much enhanced when the nanocrystals are formed in the diamond-structured phase.

The Sn-nanocrystal samples were prepared by molecular-beam epitaxy (MBE) on a Si(100) wafer ($75\text{--}125\ \Omega\cdot\text{cm}$). A 100 nm thick Si buffer layer was grown followed by a 30 nm layer composed of Si, Sn and C. The composite layer was co-deposited at 200°C at a growth rate of $0.3\ \text{\AA}/\text{s}$ and with ratios determined by secondary-ion-mass spectrometry (SIMS) to 1.6% Sn and 0.04% C. The small amount of C is added in order to reduce the strain and avoid dislocations¹⁹. Finally, a 50 nm Si capping layer was grown at a temperature of 400°C . Post-growth annealing was carried out in an N_2 atmosphere at temperatures varying from 650°C to 900°C for 20 min . in order to form the nanocrystals. Cross-sectional samples, thickness of electron transparency, were prepared for investigations by scanning transmission-electron microscopy (STEM) using a focused-ion-beam (FIB) sputtering system (FEI Versa 3D). The samples were investigated using a Talos A microscope from FEI, with a high-angle annular dark-field (HAADF) detector. Typical images for different samples, shown in Fig. 1, demonstrate that nanocrystals are formed at all the investigated annealing temperatures with only minor variations in the size distributions, see Fig. 1(h). We measure the thickness of each cross-section STEM sample by electron-energy-loss spectroscopy (EELS), which in turn allows us to determine the volume density of nanocrystals, see Fig. 3(c). The high-resolution images (insets in Fig. 1) were obtained by aligning the STEM electron beam along the $[110]$ direction and forming the image contrast by inelastic Rutherford scattering, i.e. by variations in atomic number. Hence, each spot in the image corresponds to a string of atoms, and the bright spots include Sn atoms on the string. Throughout the sample no change in lattice parameters is seen between the nanocrystals and the

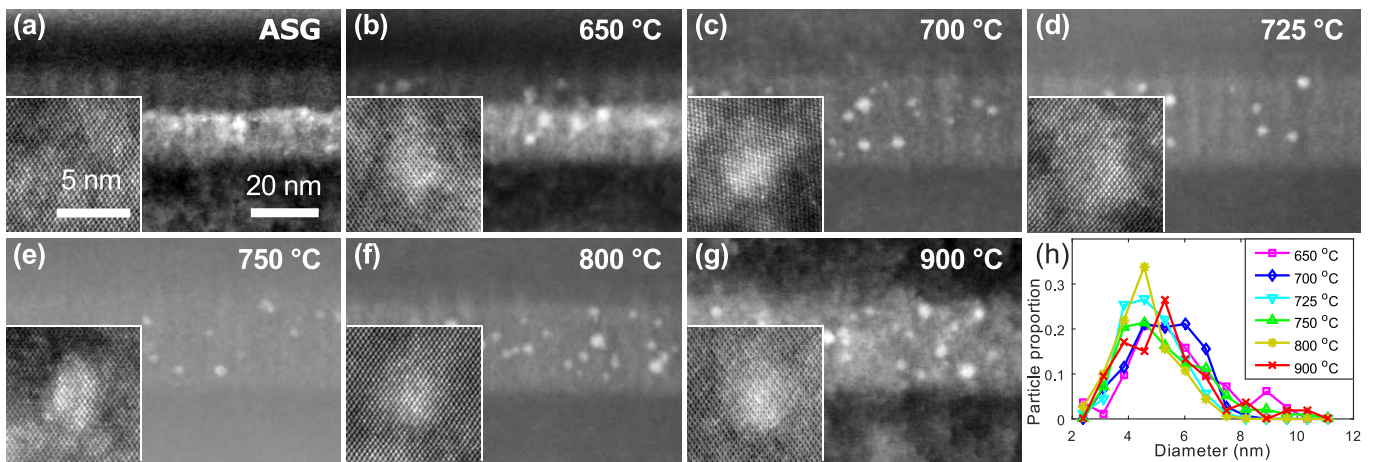


FIG. 1. STEM images of SiSnC layers as-grown (ASG) and with post-annealing. The annealing temperatures are indicated in the images. Insets show high-resolution STEM images of the nanocrystals for the respective samples. Panel (h) shows histograms of the diameter distribution for the nanocrystals based on various STEM images. The samples have different thickness and the apparent nanocrystal density is therefore not representative.

background material, and the boundary appears completely coherent.

The setup for optical investigations is identical to the one used in Ref. 20. The samples were excited by a short laser pulse of 100 fs duration and wavelength 400 nm. The light emitted from the samples was dispersed by a monochromator and measured by a photo-multiplier tube. The sample temperature during optical investigations, not to be mistaken for the annealing temperature, could be varied from room temperature down to 16 K.

The results of the optical investigations are summarized in Fig. 2. In Fig. 2(a) the photoluminescence (PL) spectra are shown for various annealing temperatures and for the as-grown (ASG) sample. We note that all samples emit some light, consistent with previous studies^{9,10} of as-grown SiSnC films. There is, however, a remarkably strong and rather broad luminescence feature centered around 0.82 eV from the sample annealed at 725 °C. Even though the center of these features depends on the annealing temperature and parts of the luminescence lie below the detection limit of 0.76 eV, it is evidently the height of each feature that is main responsible for the increased luminescence. To illustrate the overall behavior of the luminescence as a function of annealing temperature, we have calculated the area under each spectral curve, from 0.76 eV to 0.90 eV, and plotted these areas in Fig. 2(c). The strongest luminescent sample (annealed at 725 °C) has also been studied at various sample temperatures as shown by the spectra in Fig. 2(b) and the spectral areas in Fig. 2(d). The luminescent peak persists from low temperatures up to roughly 150 K.

We complement the structural STEM analysis shown in Fig. 1 by Rutherford-back-scattering spectrometry (RBS), using 2 MeV helium (He) ions, see Fig. 3. In Fig. 3(a) the broad feature below 1.4 MeV arises from Si, whereas the signal (multiplied by 10) between the vertical dashed lines originates from Sn. The left Sn peak,

centered at 1.73 MeV, corresponds to back scattering from buried Sn atoms, and the adjacent shoulder towards higher energy originates from Sn atoms at the sample surface. When the incident He ions are aligned to channel along the [001] direction, the probability of a large-angle back-scattering event will be strongly reduced. This is seen, e.g., as a reduction of the Si yield to $\chi_{\min, \text{Si}} = 4$ percent of the random yield under such channeling conditions, where $\chi_{\min, \text{Si}}$ was calculated as the channeling-to-random area under the RBS spectra in the range 1.0 MeV to 1.2 MeV. Likewise, a reduction of the peak area at 1.73 MeV (determined from a Gaussian fit) will indicate that buried Sn atoms are also suppressed by the channeling conditions and hence occupy predominately substitutional or near-substitutional sites. Calculating $\chi_{\min, \text{Sn}}$ as the channeling-to-random ratio of this peak area, shown by the black circles in Fig. 3(b), we clearly see variations in this area ratio, i.e. in the degree to which the Sn atoms are coherent with the surrounding Si lattice. A low value of $\chi_{\min, \text{Sn}} = (7.5 \pm 0.8) \%$ is observed at 725 °C, corresponding to a substitutional fraction²¹ of $S = (1 - \chi_{\min, \text{Sn}})/(1 - \chi_{\min, \text{Si}}) = (96.9 \pm 0.9) \%$, which is followed by a rapid increase to $\chi_{\min, \text{Sn}} = (25.7 \pm 1.6) \%$ at 750 °C, corresponding to a substitutional fraction of $S = (77.5 \pm 1.7) \%$. In comparison, we measure for the as-grown sample the values $\chi_{\min, \text{Sn}} = (6.1 \pm 0.8) \%$ and $S = (97.5 \pm 0.8) \%$.

The STEM data demonstrate that the variations in the nanocrystal size and number density are rather limited, taking the quite broad range of annealing temperatures into account. This is consistent with the fact that a Sn atom requires a vacancy to assist its diffusion²². These vacancies are most likely present from the initial low-temperature MBE growth process²³ and available during both the first Sn-Sn segregations steps²⁴ and the following coarse precipitation stage, which must take place at a temperature below 650 °C. In other words, for the MBE-

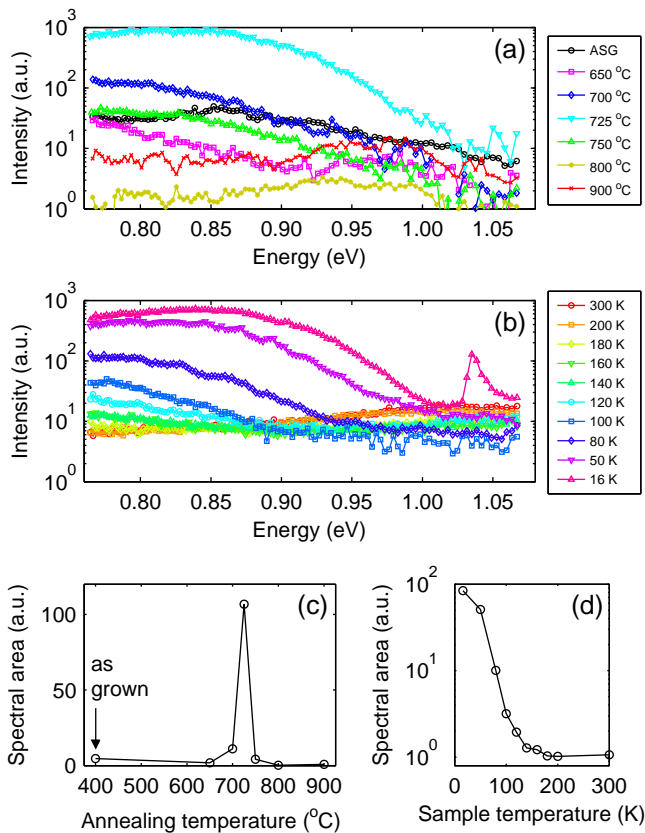


FIG. 2. (a) Time-integrated ($0 \leq t \leq 600 \mu\text{s}$) PL spectra (please note the log scale on the vertical axis), obtained from samples annealed at different temperatures and excited by a pump fluence of $\approx 8 \cdot 10^{-6} \text{ J/cm}^2$ at a sample temperature of 16 K. The area below each curve, for emission energies $E \leq 0.90 \text{ eV}$, is plotted in panel (c), showing a pronounced peak at 725 °C. Panel (b) shows the time-integrated ($0 \leq t \leq 10 \mu\text{s}$) PL spectra for the sample annealed at 725 °C, for various sample temperatures using a pump fluence of $\approx 1.5 \cdot 10^{-4} \text{ J/cm}^2$. The area below the curves, for $E \leq 0.90 \text{ eV}$, is plotted in panel (d).

grown samples, the Sn precipitation does not depend on thermally generated vacancies, which explains the limited variations in the nanocrystal size distribution on annealing temperature. Next, the different investigated annealing temperatures must lead to further maturing stages of the Sn precipitates and eventually define the conditions for the finer variations in the resulting nanocrystal structure upon cool-down to room temperature. These variations can be seen from the RBS results in Fig. 3(b), in particular in the range 700 °C to 800 °C. Evidently, for an annealing temperature of 750 °C a significant fraction of Sn atoms ends up in non-substitutional sites. It is clear from Fig. 1 that some of the Sn atoms always remain in solution within the original SiSnC layer (seen as a bright layer of thickness 30 nm in the images). However, a significant fraction of these dissolved Sn atoms cannot be located at non-substitutional sites. If they were, there would be a high probability for low-angle scatter-

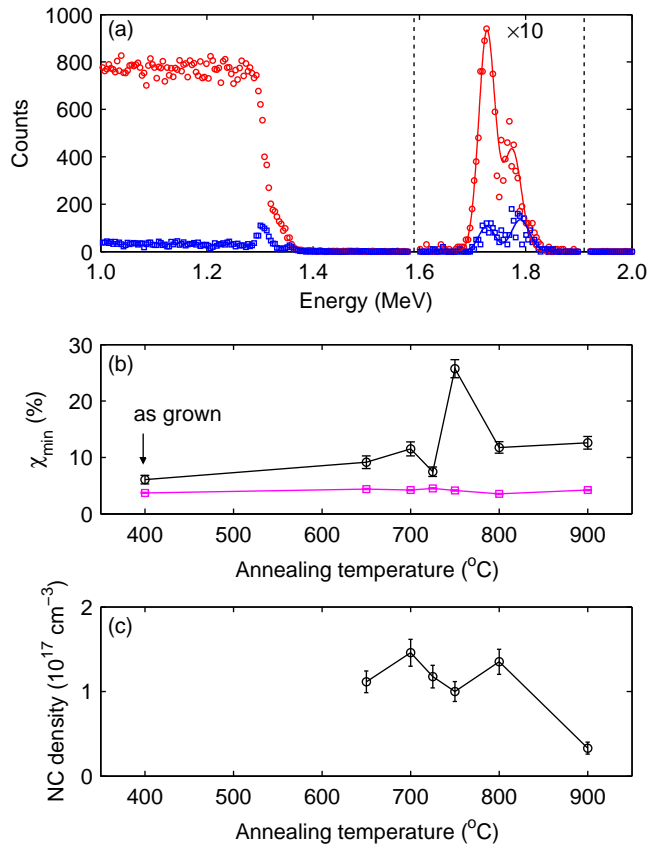


FIG. 3. (a) The measured Rutherford-back-scattering spectrum for random orientation (red circles) and under channeling conditions (blue squares) for the sample annealed at 700 °C. Solid lines are curve fits with two Gaussian peaks. Panel (b) shows $\chi_{\text{min,Sn}}$ (black circles) and $\chi_{\text{min,Si}}$ (magenta squares), as a function of the annealing temperature. Panel (c) shows, as a function of annealing temperature, the nanocrystal (NC) density determined by STEM.

ing events for all He ions passing through the Sn-rich layer. This would lead to de-channeling and accordingly a large $\chi_{\text{min,Si}}$ for back-scattering from deep Si below the SiSnC layer²¹. This is, however, not observed; the magenta squares in Fig. 3(b), representing these deep Si atoms, remain at a low value around 4 % for the sample annealed at 750 °C. Hence, the non-substitutional Sn must be located primarily within the nanocrystals. These Sn atoms will still cause de-channeling and should potentially raise the $\chi_{\text{min,Si}}$ -level for the deep Si atoms. But since the nanocrystal volume density is $\approx 10^{17} \text{ cm}^{-3}$, the area density (calculated using the 30 nm layer thickness) must be $\approx 3 \cdot 10^{11} \text{ cm}^{-2}$, and the $\approx 5 \text{ nm}$ nanocrystals will then take up only $\approx 6 \%$ of the projected area. In consequence, $\approx 94 \%$ of the He ions will never risk a low-angle scattering event, and in practice no de-channeling is observed in the Si part of the RBS spectrum.

Before we start interpreting the experimental results, it should be stressed that the amount of Sn (and C) in the nanocrystals is unknown. The low solid solubility

of Sn in Si around 0.1 %²⁵ suggests that the nanocrystals consist of pure Sn. However, even a small amount of C is known to have an impact on the Sn segregation process¹⁹, and thus possibly also on the resulting nanocrystal composition. A recent study has also indicated that the nanocrystals can exist as an SiSn alloy¹⁷. Now, for the sample annealed at 750 °C the question arises as to how the nanocrystals contain, on the one hand, non-substitutional Sn (as determined by RBS) and still, on the other hand, give rise to the coherent high-resolution images from STEM. A possible answer could be, under the assumption of a pure Sn nanocrystal, that the apparent coherence holds for an α -Sn shell and at the same time the core might be something else, possibly β -Sn, not aligned to the [110] direction and contributing a flat contrast level to the high-resolution STEM images. Along the same lines of thought, the sample annealed at 725 °C will be most likely to contain pure or high-quality α -Sn nanocrystals due to the low value of $\chi_{\min, \text{Sn}}$. It is remarkable that the variations in the nanocrystal structure, evidenced by Fig. 3(b), and the associated variations in photoluminescence intensity, evidenced by Fig. 2(c), occur in such a narrow annealing temperature range. Nevertheless, the above suggestions are consistent with previous findings from Mössbauer spectroscopy²⁶, which also demonstrated that only a narrow annealing-temperature window leads to formation of pure α -Sn nanocrystals whereas higher annealing temperatures lead to an additional formation of β -Sn. Although for significantly larger nanocrystals, it was also found in Ref. 14 that, upon cooling, molten Sn precipitates first into an α -Sn formation, coherent with the surrounding Si, followed by a β -Sn formation due to a rise of pressure. The above discussion supports the suggestion that the sharp rise in $\chi_{\min, \text{Sn}}$, at the annealing temperature of 750 °C, could have its origin in the onset of a β -Sn core. It is more unclear why the $\chi_{\min, \text{Sn}}$ decreases again at the annealing temperature of 800 °C, but it could be related to part of the Sn going back into solution, which is weakly indicated by the results of Ref. 26 and by the decreasing NC density towards 900 °C annealing temperature.

In the bulk form and at atmospheric pressure, the melting point of $\text{Si}_{1-x}\text{Sn}_x$ is known²⁷ to depend strongly on x , and the corresponding melting point in nanocrystalline form is unknown. This adds further complexity to the nanocrystal formation process and its underlying kinetics, if we assume that the Sn concentration in the nanocrystals is less than unity. Even under this assumption, however, our work concludes that the luminescence is strongest when the crystalline quality of the diamond-structured nanocrystals is highest.

Based on the optical and structural observations, one suggestion is that the light emission originates from the α -Sn or Sn-rich nanocrystals. This conjecture is consistent with the temperature-dependent PL observations, shown in Fig. 2(b,d), since the absence of light emission at high sample temperatures could reflect thermal excitation of electrons and holes into the surrounding

bulk conduction and valence bands. The center emission energy of 0.82 eV is consistent with Ref. 11 for a 5 nm α -Sn nanocrystal subjected to moderate compressive strain. Our sample, annealed at 725 °C and presumably with a crystal structure coherent with the surrounding Si, is probably subjected to a quite high compressive strain leading to a larger predicted emission energy. However, the calculations in Ref. 11 assumed the nanocrystal to be surrounded by vacuum, while our Si environment may allow for a less confined wave function and accordingly smaller confinement and emission energies. We emphasize that light emission from dislocations²⁸ in Si is unlikely, since no extended dislocations were visible in STEM. It cannot be excluded, though, that the luminescence could originate from point defects at the interface between nanocrystals and the surrounding material.

In conclusion, we have fabricated Sn-containing nanocrystals inside crystalline Si and studied their ability to emit light by photoluminescence spectroscopy. A pronounced enhancement of light emission, in a broad band centered at 0.82 eV, is found for the sample annealed at 725 °C, which is also the sample where the nanocrystals are most coherent with the surrounding Si lattice, i.e. containing Sn in a high-quality diamond-structured phase. Our results are consistent with the interpretation that light originates from the nanocrystals, although other emission mechanisms cannot be excluded.

This work was supported by the Villum Foundation. We are grateful to Bjarke R. Jeppesen for assistance with the STEM sample preparation.

- ¹R. A. Soref, Proc. IEEE **81**, 1687 (1993).
- ²M. El Kurdi, H. Bertin, E. Martincic, M. De Kersauson, G. Fishman, S. Sauvage, A. Bosseboeuf, and P. Boucaud, Appl. Phys. Lett. **96**, 041909 (2010).
- ³J. Liu, X. Sun, R. Camacho-Aguilera, L. C. Kimerling, and J. Michel, Opt. Lett. **35**, 679 (2010).
- ⁴R. Soref, J. Kouvetakis, J. Tolle, J. Menendez, and V. D'Costa, J. Mater. Res. **22**, 3281 (2007).
- ⁵S. A. Ghetmiri, W. Du, J. Margetis, A. Mosleh, L. Cousar, B. R. Conley, A. Nazzal, G. Sun, R. A. Soref, J. Tolle, B. Li, H. A. Naseem, S. A. Ghetmiri, W. Du, J. Margetis, A. Mosleh, L. Cousar, J. Tolle, B. Li, H. A. Naseem, and S.-Q. Yu, Appl. Phys. Lett. **105**, 151109 (2014).
- ⁶M. Oehme, K. Kosteki, T. Arguirov, G. Mussler, K. Ye, M. Gollhofer, M. Schmid, M. Kaschel, R. A. Körner, M. Kittler, D. Buca, E. Kasper, and J. Schulze, IEEE Photonics Technol. Lett. **26**, 187 (2014).
- ⁷S. Wirths, R. Geiger, N. V. D. Driesch, G. Mussler, T. Stolica, S. Mantl, Z. Ikonic, M. Luysberg, S. Chiussi, J. M. Hartmann, H. Sigg, J. Faist, D. Buca, and D. Grützmacher, Nat. Photonics **9**, 88 (2015).
- ⁸F. J. Guarín, S. S. Iyer, A. R. Powell, and B. A. Ek, Appl. Phys. Lett. **68**, 3608 (1996).
- ⁹A. S. T. Khan, P. R. Berger, F. J. Guarín, and S. S. Iyer, Appl. Phys. Lett. **68**, 3105 (1995).
- ¹⁰N. Wright, A. T. Khan, P. R. Berger, F. J. Guarín, and S. S. Iyer, MRS Proc. **533**, 327 (1998).
- ¹¹R. V. S. Jensen, T. Garm Pedersen, and K. Pedersen, Phys. Status Solidi Curr. Top. Solid State Phys. **8**, 1002 (2011).
- ¹²D. Kovalev, H. Heckler, M. Ben-Chorin, G. Polisski, M. Schwartzkopff, and F. Koch, Phys. Rev. Lett. **81**, 2803 (1998).

- ¹³C. Santori, D. Fattal, J. Vücković, G. S. Solomon, and Y. Yamamoto, *Nature* **419**, 441 (2002).
- ¹⁴M. F. Fyhn, J. Chevallier, A. N. Larsen, R. Feidenhans'l, and M. Seibt, *Phys. Rev. B* **60**, 5770 (1999).
- ¹⁵R. Ragan, K. S. Min, and H. A. Atwater, *Mater. Sci. Eng. B* **87**, 204 (2001).
- ¹⁶A. Karim, G. V. Hansson, W. X. Ni, P. O. Holtz, M. Larsson, and H. A. Atwater, *Opt. Mater. (Amst.)* **27**, 836 (2005).
- ¹⁷A. A. Tonkikh, N. D. Zakharov, V. G. Talalaev, C. Eisenschmidt, J. Schilling, and P. Werner, *J. Cryst. Growth* **425**, 172 (2015).
- ¹⁸I. Arslan, T. J. V. Yates, N. D. Browning, and P. A. Midgley, *Science* **309**, 2195 (2005).
- ¹⁹P. I. Gaiduk, J. L. Hansen, A. N. Larsen, F. L. Bregolin, and W. Skorupa, *Appl. Phys. Lett.* **104**, 231903 (2014).
- ²⁰B. Julsgaard, P. Balling, J. L. Hansen, A. Svane, and A. N. Larsen, *Nanotechnology* **22**, 435401 (2011).
- ²¹L. C. Feldman, J. W. Mayer, and S. T. A. Picraux, *Materials Analysis by Ion Channeling* (Academic Press, New York, 1982).
- ²²P. Kringhøj and A. N. Larsen, *Phys. Rev. B* **56**, 6396 (1997).
- ²³H.-J. Gossmann, P. Asoka-Kumar, T. C. Leung, B. Nielsen, K. G. Lynn, F. C. Unterwald, and L. C. Feldman, *Appl. Phys. Lett.* **61**, 540 (1992).
- ²⁴M. Fanciulli and J. Byberg, *Phys. Rev. B* **61**, 2657 (2000).
- ²⁵F. A. Trumbore, *Bell Syst. Tech. J.* **39**, 205 (1960).
- ²⁶C. Ridder, M. Fanciulli, A. N. Larsen, and G. Weyer, *Mater. Sci. Semicond. Process.* **3**, 251 (2000).
- ²⁷R. W. Olesinski and G. J. Abbaschian, *Bull. Alloy Phase Diagrams* **5**, 273 (1984).
- ²⁸N. A. Drozdov, A. A. Patrin, and V. D. Tkachev, *JETP Lett.* **23**, 651 (1976).